Surname *et al. Soft Sci* Year;Volume:Number
DOI: 10.20517/ss.2021.xx

Soft Science

Research Article

Flexible dual functional piezoelectric pyroelectric sensor for high temperature applications

Yinhui Li[1,2,#,*], Kai Fan[3,#], Qiguo Li[1], Jinrong Sun[3], Yuen Jin[3], Gangyi Li[1], Jianguo Liang[4], Yunlei Zhou[5], Guibin Bian[1,6,*], YongAn Huang[2,*]

[1]College of Integrated Circuits, Taiyuan University of Technology, Taiyuan 030024, Shanxi, China.

[2]State Key Laboratory of Intelligent Manufacturing Equipment and Technology, Huazhong University of Science and Technology, Wuhan 430074, Hubei, China.

[3]College of Electronic Information Engineering, Taiyuan University of Technology, Taiyuan 030024, Shanxi, China.

[4]College of Mechanical Engineering, Taiyuan University of Technology, Taiyuan 030024, Shanxi, China.

[5]Institute of Technology, Xidian University, Hangzhou 311231, Zhejiang, China.

[6]The State Key Laboratory of Multimodal Artificial Intelligence Systems, Institute of Automation, Chinese Academy of Sciences, Beijing 100190, China.

[#]These authors contributed equally to this work.

[*]**Correspondence to**: Prof. Yinhui Li, Prof. Guibin Bian College of Integrated Circuits, Taiyuan University of Technology, Taiyuan 030024, Shanxi, China. E-mail: liyinhui@tyut.edu.cn; guibin.bian@ia.ac.cn; Prof. YongAn Huang, State Key Laboratory of Intelligent Manufacturing Equipment and Technology, Huazhong University of Science and Technology, Wuhan 430074, Hubei, China. E-mail: yahuang@hust.edu.cn

Accepted Article

How to cite this article: Li, Y.; Fan, K.; Li, Q.; Sun, J.; Jin, Y.; Li, G.; Liang, J; Zhou, Y.; Bian, G.; Huang, Y. Flexible dual functional piezoelectric pyroelectric sensor for high

© The Author(s) 2021. Open Access This article is licensed under a Creative Commons Attribution 4.0 International License (https://creativecommons.org/licenses/by/4.0/), which permits unrestricted use, sharing, adaptation, distribution and reproduction in any medium or format, for any purpose, even commercially, as long as you give appropriate credit to the original author(s) and the source, provide a link to the Creative Commons license, and indicate if changes were made.

temperature applications. *Soft Sci.* 2026;6:[Accepted]. http://dx.doi.org/10.20517/ss.2025.156

Received: 31 December 2025 | **Revised:** 19 March 2026 | **Accepted:** 20 March 2026

Abstract

Prolonged operation of mechanical components under high-temperature environment severely affects their performance and service life. It is urgently needed a high-temperature resistance sensor to monitor local temperature changes in the component to enhance the safety. However, conventional sensors are difficult to simultaneously achieve excellent sensing performance and conformability at high-temperature environments for curved surfaces. Herein, a polyacrylonitrile (PAN)/zirconium acetate [$Zr(OAc)_4$]-based flexible and high-temperature-resistant piezo/pyroelectric bifunctional sensors are fabricated via heat treatment and typical package method. Incorporation of $Zr(OAc)_4$ reduced the cyclization temperature of PAN molecular chains and effectively enhanced both the mechanical properties and electrical output of the composite membranes sensor. Compared to pure PAN, the PAN/$Zr(OAc)_4$ composite nanofiber sensor (heat-treated at 450 °C) exhibits higher voltage output (~ 12.9 V) and piezoelectric sensitivity (~ 1.67 V/N) at room temperature. In addition, the sensor exhibits excellent pyroelectric output performance across a wide temperature gradient range, enabling accurate detection of engine temperature fluctuations. Remarkably, the sensor maintain stable piezoelectric and pyroelectric outputs after 5000 press-release cycles at 400 °C, highlighting its robustness under extreme conditions. These results demonstrate that PAN/$Zr(OAc)_4$ sensor provides reliable, flexible, and multifunctional solutions for real-time temperature monitoring in automobile engines, offering substantial benefits for extending engine lifespan and ensuring driving safety.

Keywords: PAN/$Zr(OAc)_4$ composite nanofiber sensors, piezo/pyroelectric bifunctionality, high-temperature resistance, flexibility, temperature warning

INTRODUCTION

In modern engineering applications such as aerospace, automotive, and energy systems, devices are often exposed to harsh service environments characterized by high

Accepted Article

temperature, high pressure, and strong vibration[1,2]. Mechanical components operate under dynamic conditions such as frequent start, stop cycles and variable loads, while components endure extreme environments of high temperature, pressure, and rotational speed[3-5]. Moreover, mechanical structures are typically complex and heterogeneous, comprising multiple materials and structural forms[6,7]. Real-time monitoring of stress, temperature, and deformation in these extreme conditions is therefore critical for ensuring operational safety and reliability.

With the advancement of sensing technology and intelligent manufacturing, sensor-based monitoring systems have become a key component of thermal management. Conventional piezoelectric sensors, while widely used for mechanical–electrical energy conversion, face significant limitations when operating at elevated temperatures or on curved and flexible surfaces. Piezoelectric materials as the key factor in improving the piezoelectric are a class of functional materials that can realize the mutual conversion of mechanical and electrical energy, and their core properties originate from the piezoelectric effect[8] and can be divided into inorganic and organic types. Inorganic piezoelectric ceramics such as barium titanate (BTO)[9-11], lithium niobate ($LiNbO_3$)[12,13], and lead zirconate titanate (PZT)[14,15] exhibit high piezoelectric coefficients and fast response, but they suffer from brittleness, low flexibility, and in some cases, environmental toxicity. Their Curie temperatures are often insufficient for high-temperature applications, and their rigid nature makes integration on flexible or complex structures difficult[16]. Organic piezoelectric polymers, including polyvinylidene fluoride (PVDF)[17-19] and poly(lactic acid) (PLA)[20-22], offer excellent flexibility and processability but possess relatively low piezoelectric constants and limited thermal stability, typically below 150 °C[23-25]. As a result, traditional piezoelectric materials struggle to simultaneously achieve high Curie temperature, high flexibility, and stable piezoelectric output at elevated temperature, restricting their use in extreme environments.

To overcome these limitations, hybrid composites combining inorganic and organic phases have been explored to leverage the high piezoelectricity of ceramics and the flexibility of polymers. Recently, Jian *et al.*[26] reported a piezoelectric nanogenerator based on polyimide (PI)/3D floral $PbTiO_3$ composites, which can harvest energy at 150 ℃. Dong *et al.*[27] investigated flexible piezoelectric energy harvesters made of KNN

Accepted Article

ceramics and PI composites with different Bi_2O_3-CoO_3 (BS) contents and measured the output performance of the energy harvesters in the temperature range of 25-300 ℃. Zhang *et al.*[28] prepared flexible piezoelectric PZT sensors on an inorganic mica substrate, which can maintain a highly stable damage detection sensitivity at 175 ℃ application temperature. However, their electrical performance and stability at elevated temperatures remain inadequate for broader engineering applications.

Polyacrylonitrile (PAN) has recently attracted attention as a promising polymer matrix due to its intrinsic piezoelectric and pyroelectric characteristics. The strong polar -C≡N groups in its molecular chain create a dipole moment of about 3.5D, enabling good piezoelectric activity[29]. After thermal treatment, PAN forms a stable conjugated ladder structure, enhancing its thermal stability to above 300 °C while retaining excellent flexibility and mechanical robustness[30]. Additionally, the material exhibits pyroelectricity after heat treatment, making it suitable for dual-mode electromechanical and thermoelectric conversion[31,32].

In this study, PAN/$Zr(OAc)_4$ membranes were fabricated via electrospinning and subjected to multi-stage heat treatment to tailor their crystalline and functional properties. The prepared sensors exhibited stable piezoelectric output across a wide temperature range (25 °C-500 °C), generating voltages of 12.9 V at room temperature and 14.1 V under high-temperature conditions. Their excellent flexibility, high sensitivity, and thermal endurance make them apply in autoengine high temperature warning and promising candidates for high-temperature flexible sensing applications, such as in oil drilling, aerospace engines, and automotive systems for real-time structural health monitoring and maintenance.

Accepted Article

EXPERIMENTAL

Materials

Specific material information is as shown in Supplementary Table 1.

Preparation of PAN/$Zr(OAc)_4$ composite nanofiber membranes

PAN powder was dissolved in DMF at a concentration of 14 wt.%. Five solutions with identical concentrations were prepared, into which $Zr(OAc)_4$ particles were added at

different mass ratios (5%, 10%, 15% and 20%) along with pure PAN control. The mixtures were continuously stirred at 3 °C for 1 h, then heated to 75 °C and maintained for 2 h to obtain homogeneous spinning solutions, the color of spinning solution is shown in Supplementary Figure 1. After degassing under vacuum, the solutions were electrospun using a 10 mL syringe with a 0.41 mm needle at 19 kV, a flow rate of 0.15 mL/h, a tip-to-collector distance of 13 cm, and a drum speed of 1000 rpm. The yield untreated PAN/$Zr(OAc)_4$ membranes were obtained after electrospinning for 8 h. Oxidative stabilization was carried out in air below 260 °C and in nitrogen above 260 °C to prevent thermal decomposition. The temperature was raised at 2 °C/min with 25 °C intervals and holding at each stage for 2 h, up to final treatments ranging from 50 to 550 °C. The heat-treated PAN/$Zr(OAc)_4$ membranes were obtained.

Preparation of PAN/$Zr(OAc)_4$ composite piezoelectric sensor

The untreated and heat-treated PAN/$Zr(OAc)_4$ membranes were cut into 1.5 × 1.5 cm^2 and sandwiched between two copper electrodes of different sizes. Wires were connected to both electrodes to serve as positive and negative terminals for output performance testing. To prevent dust, corrosion and mechanical damage for repeated testing, polyethylene terephthalate (PET) membranes were affixed to both sides of the electrodes using double-sided adhesive tape. For high-temperature testing, polytetrafluoroethylene(PTFE) was used as the encapsulation material instead of PET.

Room-temperature testing

The electrical output of the composite piezoelectric sensor at room temperature was evaluated using a test platform. The open-circuit voltage and short-circuit current were recorded at room temperature under a vibration frequency of 10 Hz and a constant applied force of 8 N.

High-temperature testing

The piezoelectric performance of the assembled composite sensor was further characterized at elevated temperature (200 ℃, 260 ℃, 300 ℃, and 350 ℃) using a custom-built high-temperature test platform in our lab[33]. The high-temperature test platform was constructed by a bidirectional temperature controller, two galvanically coupled copper plates

Accepted Article

Characterization

The surface morphology and internal structure of fibrous membranes were characterized by cold field emission scanning electron microscopy (SEM, Hitachi SU8010, Japan). The crystalline structures were measured by X-ray diffraction (XRD, Rigaka Smart Lab SE, Japan) with a Cu Kα radiation (λ = 1.54060 Å), a scanning range from 5° to 80°, and a scanning speed of 10 °/min. Fourier transform infrared spectroscopy (FTIR, Thermo Scientific Nicolet iS20, USA) was employed to record the spectra in the range of 400 to 4000 cm^{-1}. Differential scanning calorimetry (DSC, DSC25, TA, USA) was performed under a N_2 atmosphere with a heating rate of 10 ℃/min up to 350 ℃. Thermogravimetric analysis (TGA, TGA-50, Shimadzu, Japan) was conducted to evaluate the thermal stability and heat loss behavior of the composite nanofiber membranes with the heating rate of 10 ℃/min up to 800 ℃ under N_2 atmosphere flow. The polarization-electric field (P-E) hysteresis loops of the composite membrane were measured using a ferroelectric analyser (RTI-Multiferroic, Radiant, Technologies, USA). The dielectric constant (ε_r) and dielectric loss (tanδ) in the frequency range of 100 Hz to 1,000,000 Hz were characterized using an LCR meter (Model 2110, Keithley, USA). Specific instrument information as shown in Supplementary Table 2.

RESULTS AND DISCUSSION

Characterization of morphology, structure, mechanics and thermal behavior

Figure 1 shows comprehensive structural, morphological, and functional characterization of PAN/$Zr(OAc)_4$ composite nanofibers under varying heat treatment conditions. The color transformation of PAN/$Zr(OAc)_4$ membranes under different heat treatment temperatures is shown in Figure 1A. From Figure 1A, when the heat-treated temperature is below 260 ℃, the membrane color gradually changes from white to light yellow. For the heat-treatment temperatures of 260 °C and higher, the color shifts from light yellow to brown, and further increases to 450 ℃, the composite membrane appearing nearly black. This phenomenon arises from the structural transformations of the PAN molecular chains during thermal treatment. Initially, cyclization and cross-linking reactions occur, and above 260 ℃, polymerization between cyano(-C≡N) leads to the formation of conjugated aromatic network structures. The growth of these conjugated structures enhances light absorption, causing the membrane to darken. With further temperature

Accepted Article

elevation, carbonization begins, during which hydrogen and oxygen are gradually released in the form of H_2O and CO_2. As the degree of carbonization increases, the carbon content of the membrane rises significantly, leading to the observed black appearance[34,35]. To evaluate the flexibility and tensile properties of PAN/$Zr(OAc)_4$ membrane in comparison with conventional rigid sensors, the results are presented in Figure 1C. Both rigid(PZT5 bimorph) and flexible PAN/$Zr(OAc)_4$ composite sensor can adhere well to flat surfaces; however, on curved surfaces, the rigid sensor fails to conform completely, leading to reduced measurement accuracy. In contrast, the flexible PAN/$Zr(OAc)_4$ composite sensor can achieve full contact with curved surfaces, thereby maintaining reliable test results. Furthermore, from Supplementary Figure 2, the PAN/$Zr(OAc)_4$ composite nanofiber membranes could be subjected to multiple folding tests, after which they consistently recovered to their original state without damage. Compared to pure PAN nanofiber membrane exhibited fractures at the folded regions after repeated bending, indicating that the incorporation of $Zr(OAc)_4$, significantly enhances the flexibility and deformability of the composite membranes. The morphology of electrospun PAN/$Zr(OAc)_4$ composite nanofiber membrane under untreated (25 ℃) and after heated at different temperature (150 ℃, 260 ℃, 350 ℃, 450 ℃, 550 ℃) and corresponding diameter distribution histograms of the fibril structures are shown in Figure 1D and E. As observed in Figure 1D, the electrospun membranes exhibit well-oriented fibers with smooth surfaces and uniform distribution. With increasing heat-treatment temperature, the fiber diameter gradually decreases.The average fibril diameter gradually decreases from 0.473 μm to 0.286 μm when the treated temperature increases from 25 ℃ to 550 ℃. Additionally, when the heat treatment temperature reaches 550 °C, partial fiber fracture and aggregation occur, which may obstruct charge-transport pathways and consequently influence the electrical properties of the membranes. Although the fibrous diameter of the PAN/$Zr(OAc)_4$ membrane decreased after heat treatment, the overall fiber morphology remains largely unchanged.

Accepted Article

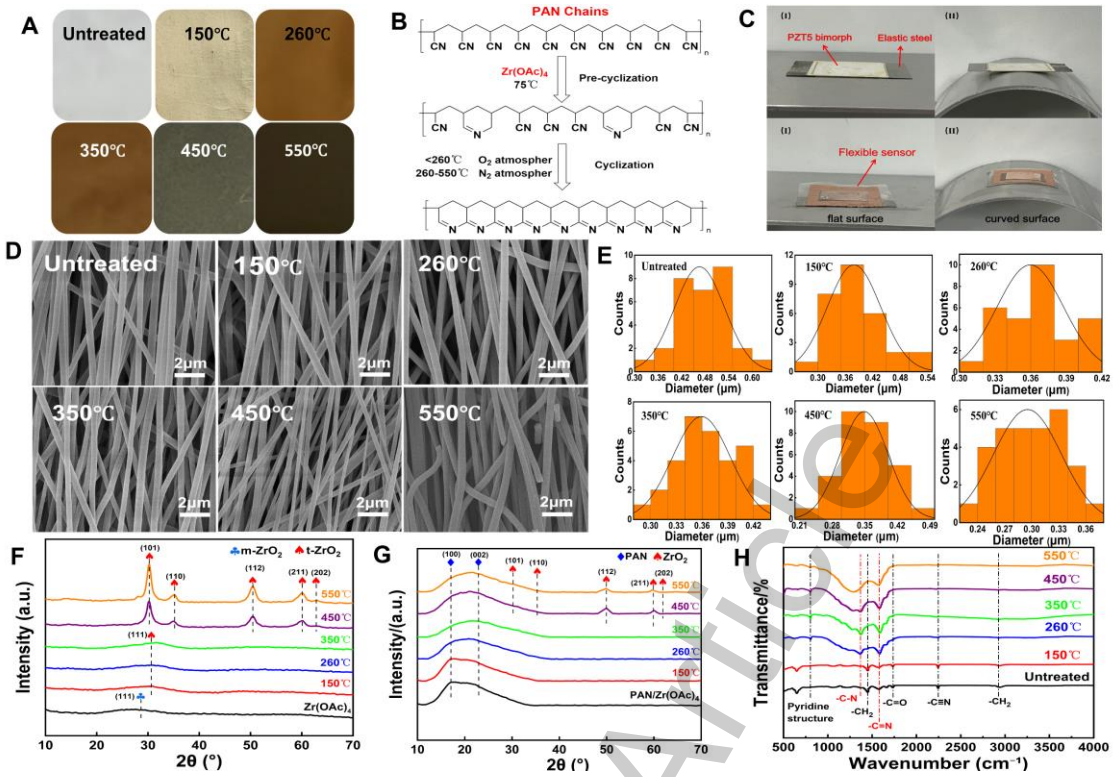

Figure 1. Characterization of PAN/$Zr(OAc)_4$ nanofiber membranes at different heat-treated temperatures. (A) The color transformation of PAN/$Zr(OAc)_4$ membranes at different heat treatment temperatures; (B) Mechanistic effect of $Zr(OAc)_4$ incorporation on PAN molecular chains under heat treatment conditions; (C) Comparison of conformability for PAN/$Zr(OAc)_4$ composite nanofiber flexible sensors with conventional PZT rigid sensors, i and iii pasted sensor on flat surface; ii and iv pasted sensor on curved surface; (D) SEM images of PAN/$Zr(OAc)_4$ at different heat treatment temperatures: untreated, 150 °C, 260 °C, 350 °C, 450 °C, 550 °C; and (E) histogram of diameter distribution. XRD patterns of (F) $Zr(OAc)_4$ particles and (G) PAN/$Zr(OAc)_4$ membranes at untreated and different heat treatment temperatures; (H) FTIR spectra of PAN/$Zr(OAc)_4$ membranes at different heat treatment temperatures.

Accepted Article

In addition, the reduced fiber diameter facilitates oxygen diffusion into the fibers, thereby enhancing the degree of PAN cyclization and promoting the cyclization reaction[36].

The crystal structure evolution of $Zr(OAc)_4$ powder and PAN/$Zr(OAc)_4$ composite nanofiber membrane under different temperature treatment (untreated, 150 °C, 260 °C, 350 °C, 450 °C, 550 °C) was characterized using XRD, and the results are shown in Figures 1F and G. As illustrated in Figure 1F, diffraction peak at $2\theta \approx 28.2°$ corresponds

to (111) crystal plane is the reflections of monoclinic polymorph, and the diffraction peak at 2θ ≈ 30.2° corresponds to (111) crystal plane observed treated temperature from 150 to 350 ℃ is the reflection of tetragonal polymorph[37]. The XRD indicated that crystalline structure occurred with monoclinic-to-tetragonal transition. Furthermore, diffraction peaks at 2θ ≈ 30.2°, 35.2°, 50.3°, 60.1°, and 62.5° are generated as the heat treatment temperature increases to 450 °C and 550 °C, correspond to the (101) (110) (112) (211) and (202) facets of zirconium oxide (ZrO_2), respectively, which are consistent with the crystal structure of tetragonal-phase zirconium oxide on JCPDS(No.80-0965) cards[38]. This phenomenon suggests that $Zr(OAc)_4$ has already decomposed into ZrO_2 production when the heat treatment temperature reaches 450 °C. From Figure 1G, a diffraction peak was observed at 2θ ≈ 17° for the untreated PAN/$Zr(OAc)_4$ composite nanofibers, which was identified as (100) diffraction from the hexagonal lattice of PAN. As the heat treatment temperature increases, the diffraction peak of PAN/$Zr(OAc)_4$ near 2θ ≈ 17° begins to shift to right, and a new broad peak appears near 2θ ≈ 23°, which is attributed to the creation of (002) crystalline facets of the aromatic planar structure of the carbon network (also known as the graphite-like structure) due to the cyclisation reaction of PAN[39]. When the heat treatment temperature reached 450 °C, the diffraction peaks corresponding to the crystal planes of ZrO_2 appeared. These diffraction peaks gradually became pronounced with increasing temperature, indicating that the thermal decomposition of $Zr(OAc)_4$ and the subsequent formation of crystalline ZrO_2 at high temperature. With increasing heat-treatment temperature, not only the aromatic planar structure of the PAN carbon network, but also the generation of piezoelectric ceramics ZrO_2 which might be the significant factors for the enhancement of the electrical properties of the PAN/$Zr(OAc)_4$ membranes.

The FTIR spectra of PAN/$Zr(OAc)_4$ composite nanofiber membranes before and after heat treatment at 150 °C, 260 °C, 350 °C, 450 °C and 550 °C are shown in Figure 1H. For the untreated PAN/$Zr(OAc)_4$ fiber membranes, several distinct absorption peaks of PAN functional groups can be seen in the FTIR spectrum, which correspond to stretching vibrations of C-H in -CH_3 near 2,927 cm^{-1}, -C≡N(cyano) near 2,242 cm^{-1}, -C=O near 1,731 cm^{-1}, and the bending vibration of C-H in -C=H_2 at 1,450 cm^{-1}[40,41]. As the heat treatment temperature increases, the characteristic stretching peak of C-H in in -CH_3 near 2,927 cm^{-1} and the bending vibration peak of C-H in -C=H_2 near 1,450 cm^{-1} gradually disappear, indicating that dehydrogenation occurs on the main PAN chain with the loss

Accepted Article

of hydrogen atoms. Simultaneously, the cyano group -C≡N (~ 2,242 cm^{-1}) featured of the PAN structure disappeared and formed into -C=N (~ 1,575 cm^{-1}) and -C-N (~ 1,373 cm^{-1}), together with pyridine structure absorption peak near 806 cm^{-1} corresponding to a six-membered ring structure, suggest that cyclization takes place along the PAN backbone. This transformation converts the disordered helical supramolecular structure into a planar, thermally stable ladder-like structure[42,43]. It is worth noting that the -C=N absorption peak near 1,575 cm^{-1} has already observed in the untreated PAN/$Zr(OAc)_4$ membrane, which suggests that the incorporation of $Zr(OAc)_4$ induces a pre-cyclisation reaction of the PAN molecular chain during the spinning solution preparation. Specifically, $Zr(OAc)_4$ can be decomposed into free ions at elevated temperatures., the generated nucleophile CH_3COO^- ions attack the positively charged carbon atoms in the -C≡N groups, initiating a partial pre-cyclization process on the PAN molecular chains[44].

The stress-strain curves of pure PAN and PAN/$Zr(OAc)_4$ composite nanofiber membranes without heat treatment are shown in Figure 2A. From the Figure 2A, the tensile strength PAN nanofiber membrane and PAN/$Zr(OAc)_4$ membrane are 5.23 and 7.84 MPa, and the elongation at break is 4.9% and 9.8%, respectively. The introduction of $Zr(OAc)_4$ could simultaneously enhance the stress and break elongation, and the increment of stress and break elongation are 49.2% and 100.0% respective. This may be attributed to the formation of an ionic cross-linked network between Zr^{4+} and the -C≡N in PAN[45], which simultaneously enhances the tensile strength and elongation at break of the fibers. Furthermore, from Figure 2B, the tensile strength PAN nanofiber membrane and PAN/$Zr(OAc)_4$ membrane after heat treatment at 260 ℃ are 9.28 and 14.36 MPa, and the elongation at break is 3.4% and 4.8%, and the increment of stress and break elongation are 54.7% and 41.2% respective, which is due to the chemical cross-linking and cyclisation of PAN molecular chains induced by the 260 °C heat treatment, transforming them from linear thermoplastic polymers into rigid ladder-type thermosetting structures[46]. The column comparison results of stress and break elongation are for pure PAN nanofiber membrane and PAN/$Zr(OAc)_4$ membrane are shown in Figure 2C. The above results indicate that the introduction of $Zr(OAc)_4$ enhances the various mechanical properties of nanofiber membranes.

In order to investigate the effect of $Zr(OAc)_4$ incorporation on the thermal behavior of

Accepted Article

PAN nanofibers, PAN/$Zr(OAc)_4$ composite nanofiber membranes were characterized by TGA and DSC at different heat treatment temperatures, and the results are shown in Figure 2D-I. Figure 2D and E present the thermal weight loss of different heat treatment temperatures PAN/$Zr(OAc)_4$ membranes. The untreated nanofiber membrane curves have 2 obvious weight loss near 98 and 287 ℃, the first one may be due to the volatilization of residual moisture and solvents within the composite nanofiber membrane, with no significant chemical decomposition occurring, and the second reason can be attributed to the cleavage of acrylonitrile groups along the PAN molecular chains, representing the core reaction in PAN thermal stabilization. As the heat treatment temperature increases, the thermal weight loss time of the membrane gradually shifts to the right, indicating that the heat-treated nanofiber membranes have higher thermal stability than the untreated one. The carbon yield and onset temperature are shown in Supplementary Table 3, the residual carbon yield of the heat-treated nanofiber membrane at 550 ℃ is 70.1% , which is a significant enhancement compared with the untreated one(40.1%). High carbon yield enables membranes to form a more complete conjugated structure, improving the mechanical properties of the fiber membranes.

According to the DSC curves in Figure 2F, the exothermic peak of the untreated PAN/$Zr(OAc)_4$ composite nanofiber membranes is found to be 2.65 °C lower than that of the pure PAN nanofiber membrane. This shift could be attributed to the formation of "π- π" interactions between CH_3COO^- in $Zr(OAc)_4$ and the strong polar -C≡N group in PAN,which weaken the intermolecular forces among the -C≡N groups in the amorphous regions of PAN[47].

Accepted Article

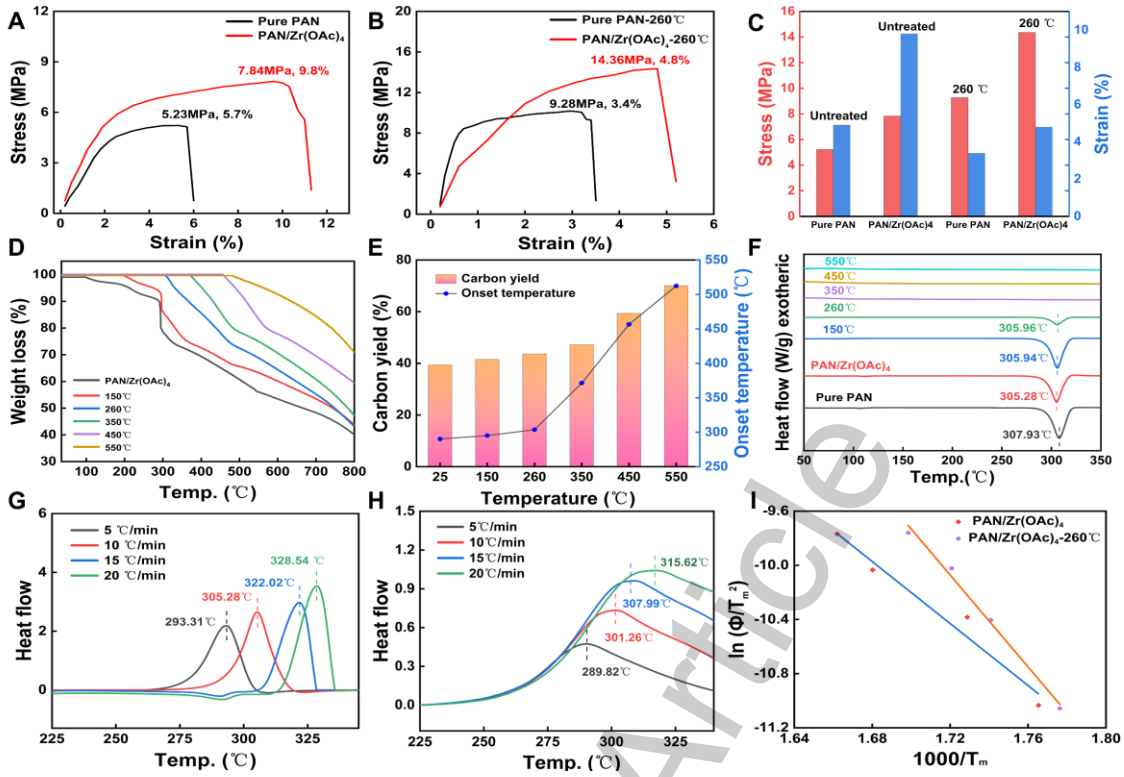

Figure 2. Stress-strain curves of pure PAN and PAN/Zr(OAc)$_4$ composite nanofiber membranes. (A) Untreated and (B) 260 °C heat-treatment; (C) Comparison of stress and strain for pure and composite films untreated and 260 °C heat-treatment. (D) TGA curves of untreated and different heat treatment temperatures PAN/Zr(OAc)$_4$ membranes from 50 °C to 800 °C at a heating rate of 10 °C min^{-1} under N_2. (E) Column comparison chat of carbon yield and onset temperature for different heat treatment temperature PAN/Zr(OAc)$_4$ nanofiber membrane. (F) DSC curves of pure PAN versus PAN/Zr(OAc)$_4$ membranes from 50 to 350 °C under N_2 with different heat treatment temperatures. DSC curves of PAN/Zr(OAc)$_4$ membranes at different heating rates: (G) untreated; (H) 260 °C heat-treatment and (I) plot of $\ln(\Phi/T^2_m)$ versus $1000/T_m$ according to the Kissinger.

As a result, more planar zigzag conformations are formed, facilitating the cyclization reaction. The exothermic peak begins to gradually shift toward higher temperatures at heat treatment temperatures between 150 and 350 °C, which may be due to the decomposition of Zr(OAc)4 weakening the 'π-π' interactions. There is no exothermic peak is observed above 350 °C, as the carbonized membrane structure achieves enhanced stability, effectively suppressing exothermic reactions[48]. Specifically, the cyclization reaction of PAN is advanced to below 350℃ with the acceleration of Zr(OAc)$_4$, and the cyclization process further leads to the formation of stable ladder-type polymers from the

Accepted Article

fracture of PAN microcrystalline structure; meanwhile, the decomposition of $Zr(OAc)_4$ at high temperatures (overlapping with the temperature range of PAN ladder polymerisation) exhibits weakly exothermic or slightly endothermic characteristics, which counteracts and masks the residual exothermic signal, collectively resulting in the absence of exothermic peak above 350 ℃. The decomposition trend of $Zr(OAc)_4$ is in good agreement with the XRD pattern. Lowering the cyclization temperature can effectively suppress the thermal weight loss of PAN/$Zr(OAc)_4$ membranes during the heat stabilization process. When the heat treatment temperature increases, the exothermic peak of the fiber membrane gradually shifts to the right, which may be caused by the partial CH_3COO^- decomposition. In addition, it can be seen from the figure that the exothermic peak exhibits a sharp peak, the heat transfer during the cyclization reaction takes place instantaneously rather than through a gradual chain process[49]. Figure 2G-H are DSC curves of PAN/$Zr(OAc)_4$ membrane with untreated and heat treatment of 260 ℃ at different heating rates(5, 10, 15, 20 ℃/min), respectively. The apparent activation energy (E_a) of the cyclization reaction was determined by Kissinger method and the following Equation (1):[50]

$$\frac{E_a}{R} = -\frac{d[\ln(\frac{\Phi}{T_m^2})]}{d(\frac{1}{T_m})} \quad (1)$$

where Φ is the heating rate, T_m represents the peak temperature, and the value of E_a corresponds to the slope of the linear curve of $\ln(\Phi/T^2_m)$ and $1000/T_m$. For the Kissinger analysis, linear regression was performed to verify the reliability of the fitting results, and the linear correlation coefficient (R^2) was greater than 0.99, indicating excellent fitting validity. In Figure 2I, the E_a values of the untreated PAN/$Zr(OAc)_4$ and the 260 ℃ treated membrane were calculated to be 11.447 ± 0.321 kJ·mol^{-1} and 16.974 ± 0.458 kJ·mol^{-1}, respectively (the uncertainty was expressed as the standard deviation of three parallel measurements). The significant increase in E_a after heat treatment at 260 ℃ can be attributed to the combined effects of constrained chain mobility and enhanced structural ordering of the PAN molecular chains. The heat treatment at 260 ℃ promotes the partial cyclization of PAN molecular chains and the rearrangement of molecular segments, which enhances the crystallinity of the fiber membrane and induces a more orderly arrangement of molecular chains. This ordered structure restricts the segmental

Accepted Article

motion of PAN chains, making it difficult for the molecular chains to undergo further cyclization reactions[51]. As a result, a higher energy barrier needs to be overcome to initiate the cyclization reaction, leading to an increase in the apparent activation energy. High activation energy represents good thermal stability, which can prevent chain breakage and fiber melting due to the rapid evolution[52].

Electrical properties and stability

In order to investigate the effect of doping concentration of $Zr(OAc)_4$ on the performance of composite nanofiber membranes, the output open-circuit voltages and short-circuit currents of PAN/$Zr(OAc)_4$ membranes containing different mass fractions (0, 5, 10, 15, and 20 wt%) doping on PAN/$Zr(OAc)_4$ membranes were measured respectively and the testing results are shown in Supplementary Figure 3. From the Supplementary Figure 3, it can be seen that the output open-circuit voltage of this flexible piezoelectric sensor gradually increases with the increasing of $Zr(OAc)_4$ content, and the output open-circuit voltage reaches the optimum value of 12.9 V under an external force of 8 N when the filler reaches 10 wt.%, and the output voltage of the piezoelectric sensor starts to decrease when the content of $Zr(OAc)_4$ continues to increasing, which may be due to the fact that too much doped filler makes the composite material internal agglomeration occurs, leading to the deterioration of the electromechanical coupling effect, which results in a lower output voltage. The output short-circuit current of this piezoelectric sensor exhibits the same trend as the output voltage, the peak output current reaches 350 nA at a mechanical external force of 8N when the content of $Zr(OAc)_4$ reaches 10 wt.%. Doping with fillers with a content of 10 wt% was used in subsequent studies and experimental applications.

To investigate the electrical properties of PAN/$Zr(OAc)_4$ composite nanofiber membranes, the output open-circuit voltages and short-circuit currents of the fiber membranes were tested at room temperature environment for untreated and different heat treatment temperatures as shown in Figure 3A-C. Figure 3A shows that the occurrence of thermal cyclization reaction converts the disordered helical supramolecular structure into a planar heat-resistant trapezoidal stabilized structure when the heat treatment temperature is in the range of 50-260 ℃, and the change of the output voltage of the piezoelectric membrane has roughly the same trend as that of the pure PAN nanofiber

Accepted Article

membrane, but the PAN/$Zr(OAc)_4$ composite piezoelectric membrane outperforms the pure PAN piezoelectric membrane in all temperature gradients. When the heat treatment temperature is higher than 260 ℃, the heat treatment environment of the fiber membrane is under nitrogen atmosphere, which can slow down the carbonization of the fiber membrane to a certain extent, leading to the generation of graphite-like structure, so that the piezoelectric properties are reduced. The piezoelectric output characteristics of the PAN/$Zr(OAc)_4$ membrane were dramatically enhanced when the heat treatment temperature reached 450 °C and above, with a maximum output voltage of 12.9 V, which was 1.33 times higher than the peak voltage of the pure PAN piezoelectric membrane (9.7 V). From Figure 3B, the trend of the output short-circuit current is approximately the same as that of the output open-circuit voltage, and the output peak current of the PAN/$Zr(OAc)_4$ membrane is 350 nA, which is 1.22 times higher than that of the PAN piezoelectric membrane (286 nA), due to the increase in the number of ZrO_2 nanoparticles produced by thermal decomposition of $Zr(OAc)_4$, which results in the membrane's piezoelectric properties to improve. When the temperature is increased to 550 °C, according to SEM, it can be found that the internal fibers of PAN/$Zr(OAc)_4$ undergo fracture, which leads to a decrease in the degree of cyclization and the generation of more graphite-like structures, resulting in a decrease in the piezoelectric properties. Figure 3C shows the line graphs of the output voltage and current of the membrane at different heat treatment temperatures, which more intuitively shows the trend of the output voltage and current. In addition, according to Supplementary Figure 4, a mechanical external force of 2-10 N was applied to the sensor and increased in this way at intervals of 2 N. It was found that the output voltage showed a good linear response with pressure and the output voltage sensitivity was 1.67 V/N, which was 63.5% higher than that of the pure PAN nanofiber sensor. This reflects the outstanding pressure-responsive characteristics of the PAN/$Zr(OAc)_4$ membrane sensor.

Accepted Article

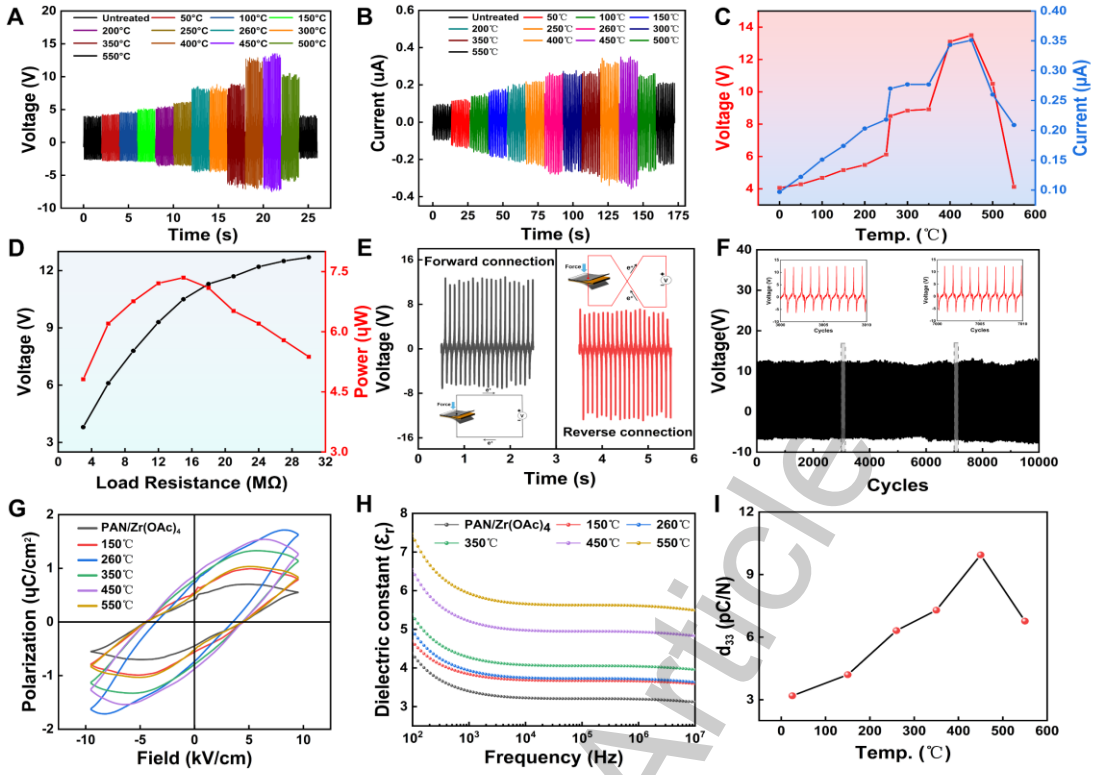

Figure 3. Piezoelectric performance of the PAN/Zr(OAc)$_4$ composite nanofiber membrane sensor at different heat-treatment. (A) Dependence of open-circuit voltage and (B) short-circuit current. (C) Voltage and current line graphs. (D) Voltage and instantaneous power of the sensor at different external load resistances. (E) Polarity reversal test of the sensor. (F) Stability test under 10,000 cycles. PAN/Zr(OAc)$_4$ composite membranes untreated and at different heat treatment temperatures under room temperature conditions (~25 °C): (G) ferroelectric properties (P-E); (H) dielectric constant and (I) piezoelectric coefficient d_{33} curve.

Based on the above experimental data, the electrical properties of PAN/Zr(OAc)$_4$ composite nanofiber membranes can be significantly improved after high-temperature heat treatment, and it is expected that the membranes can be used in the fields of flexible sensing and detection, and flexible electronic skin wear.

Figure 3D shows the PAN/Zr(OAc)$_4$ output voltage by testing the output voltage of PAN/Zr(OAc)$_4$ composite nanofiber membrane with external load resistors, which are 3, 6, 9, 12, 15, 18, 21, 24, 27, and 30 MΩ, and the output voltage is increased from 3.8 V to 13.1 V. At the same time, the instantaneous output power is calculated using Equation(2):

Accepted Article

$$P = \frac{U^2}{R} \quad (2)$$

Where U is the voltage at both ends of the PAN/$Zr(OAc)_4$ membrane with external load, and R is the external load. When the external load is 15 MΩ, the output power is taken as the maximum value of 7.35 μW. The maximum output power is achieved when the internal resistance of the sensor matches the external load. On this basis, the internal resistance of the PAN/$Zr(OAc)_4$ membrane sensor is determined to be approximately 15 MΩ

To further verify the validity of the piezoelectric effect, the polarity reversal test was carried out on PAN/$Zr(OAc)_4$ composite nanofiber membranes, as shown in Figure 3E. When the membrane was connected to the test circuit in the forward direction, a positive signal was detected with voltage wave peaks and troughs of 12.9 V and -7.3 V, respectively. Conversely, when the membrane was connected to the test circuit in the reverse direction, voltage wave peaks and troughs of 7.1 V and -12.6 V were detected. As a result, the peaks of the PAN/$Zr(OAc)_4$ membrane are opposite in positive and negative values under forward and reverse connections, but equal in magnitude, which indicates that the voltage output signal is indeed generated by the piezoelectric effect, and does not belong to the external disturbances or friction electric effect. In addition, the stability of PAN/$Zr(OAc)_4$ membranes was also tested by knockdown tests, as shown in Figure 3F. The 450 ℃ heat-treated composite fibrous membrane sensing device was tested to 10,000 cycles, and it was observed that the output performance remained unchanged and was almost stable at around 12.9 V without significant fluctuations. This indicates that the prepared PAN/$Zr(OAc)_4$ flexible piezoelectric sensing device has good stability and is able to continuously convert mechanical properties into electrical energy, which can be used for sensing and detecting mechanical motion at room temperature. Table 1 summarizes and compares the normalized electrical output performance (e.g., sensitivity per unit force) and maximum operating temperature of different high-temperature piezoelectric materials under high-temperature environments. The PAN/$Zr(OAc)_4$ composite piezoelectric sensors in this study exhibit superior normalized electrical performance and a higher operating temperature compared to most reported counterparts. However, it should be noted that the benchmarking comparison is still

Accepted Article

limited by the inconsistent ambient testing temperatures adopted in different reports. Since the sensing performance of piezoelectric and pyroelectric materials is generally temperature-dependent, the lack of uniform testing temperature among different sensors brings potential deviations to the comparison. Therefore, the above comparison can only provide a preliminary reference for performance evaluation, rather than an absolute quantitative judgment.

Table 1. Electrical output and maximum operating temperature of different piezoelectric materials at elevated temperatures

Piezoelectric material	**Sensitivity （V/N）**	**Voltage（V）**	**Maximum operating temperature/°C**	**Ref**
PSN-PZT	0.035	6.834	184	[56]
PZT-5H	0.032	3	200	[57]
GaN	0.61	0.12	300	[58]
ITO/In_2O_3	0.18	-	300	[59]
PI/ZnO	0.75	4	500	[60]
PAN/$Zr(OAc)_4$	1.67	12.9	500	This work

In order to further investigate the effect of how the introduction of $Zr(OAc)_4$ affects the piezoelectric output characteristics of PAN/$Zr(OAc)_4$ composite nanofiber membrane sensors. The residual polarization strength (P_r) of the membranes at room temperature (~ 25 °C) and the dielectric constant (ε_r) in the frequency range of 102-106 Hz were tested for the untreated and different heat treatment temperatures (150 °C, 260 °C, 350 °C, 450 °C, and 550 °C). From Figure 3G, the value of the residual polarization strength P_r gradually increased from 0.42 μC/cm^2 to 0.73 μC/cm^2 as the heat treatment temperature increased from 25 °C to 260 °C. When the heat treatment temperature was between 260 °C and 450 °C, the overall change of the residual polarization strength P_r was not significant and was stable at 0.8 μC/cm^2 or so, but when the heat treatment temperature was increased to 550 °C, the residual polarization strength decreased to 0.52 μC/cm^2. The change of the P_r value of the residual polarization strength indicates that the increase of the heat treatment temperature can make the internal polarization state of the

Accepted Article

membrane more stable and oriented more consistently, which in turn improves the energy conversion efficiency of the piezoelectric sensor.

As shown in Figure 3H, due to the Maxwell-Wagner-Sillars polarization effect[53,54]that makes the composite material under the action of alternating electric field, the charge accumulation at the interface between its organic and inorganic phases, resulting in the ε_r of PAN/$Zr(OAc)_4$ composite nanofiber membrane sensors under different heat treatment temperatures decreases gradually with the increase of the test frequency, and with the increase of the heat treatment temperature, the ε_r value gradually increases. When the heat treatment temperature was increased from 150 °C to 550 °C, the ε_r values of PAN/$Zr(OAc)_4$ membranes were elevated from 4.61 to 7.30 at the test frequency of 100 Hz, and all of them were higher than those of the untreated membranes (ε_r = 4.28). According to the results, the heat-treated PAN/$Zr(OAc)_4$ membrane has a high dielectric constant and low dielectric loss [Supplementary Figure 5], which enables the material to accumulate more charge under the same electric field and lose less energy during charging and discharging, and has an excellent charge storage capability.

It is well known that the piezoelectric properties of piezoelectric materials are determined by the piezoelectric coefficient d_{33}, which is related to the magnitude of the residual polarization strength P_r and the dielectric constant ε_r, and d_{33} is calculated by Equation (3):[55]

$$d_{33} = 2Q_{11}\varepsilon_0\varepsilon_r P_r \quad (3)$$

where ε_0 is the vacuum dielectric constant (ε_0 = $8.854\times10^{-12}F\cdot m^{-1}$), which is the electrostriction constant of the cis-phase in the range of (0.05-0.1 $m^4\cdot C^{-2}$). The calculation result of d_{33} are shown in Figure 3I, it was found that the trend of the piezoelectric coefficient d_{33} was consistent with the output voltage and current of the PAN/$Zr(OAc)_4$ membranes, which indicated that the addition of $Zr(OAc)_4$ had a significant effect on the enhancement of piezoelectric properties. The output voltages, output currents, the residual polarizable strengths P_r, the dielectric constants ε_r, and the piezoelectric coefficients of the PAN/$Zr(OAc)_4$ membranes The values of d_{33} are shown in Table 2.

In order to validate the high-temperature resistance of the fiber membranes, the

Accepted Article

PAN/$Zr(OAc)_4$ composite nanofiber membranes (heat-treated at 450 ℃) were tested at four high temperature conditions, 200 ℃, 260 ℃, 300 ℃, and 350 ℃, the infrared thermogram of the high temperature environment tested as shown in Figure 4A . All piezoelectric measurements were performed under a mechanical force of 8N (applied at an excitation frequency of 10 Hz), with an effective active sensor area of 2.25 cm^2 (1.5 cm × 1.5 cm) and a membrane thickness of 120 μm. For electrical connections at elevated temperatures, high-temperature-resistant nickel (Ni) wires and conductive copper tape were used to ensure stable contact. Voltage signals were captured via an external oscilloscope. At different high temperature conditions, the peak output voltage were 13.7V, 14.1V, 13.4V and 13.9V, respectively [Figure 4B], the output voltage remains almost constant at high temperatures [Figure 4C], and is consistent with the result tested at room temperature. This show that the fabricated sensor can be used in high-temperature environments. Furthermore, to test the long-term stability under high-temperature exposure, the sensor was subjected to isothermal static tests at 350 °C for 100, 200, 300, and 400 h, respectively. After different durations of testing, the peak output voltage did not show significant reduction or fluctuation, indicating that the fabricated sensor can be used in a high-temperature environment for long-term static operation [Supplementary Figure 6]. In addition, a polarity reversal test was also carried out on the fiber membrane in a high temperature environment (the test environment is 400 ℃), respectively, the fiber membrane sensor was connected positively and negatively in the measurement circuit, and a positive and negative signal was obtained from the measurement shown in Figure 4D. The measurement results show that the output voltage originates from the piezoelectric signal generated by the PAN/$Zr(OAc)_4$ membrane sensor during mechanical force loading and unloading.

Accepted Article

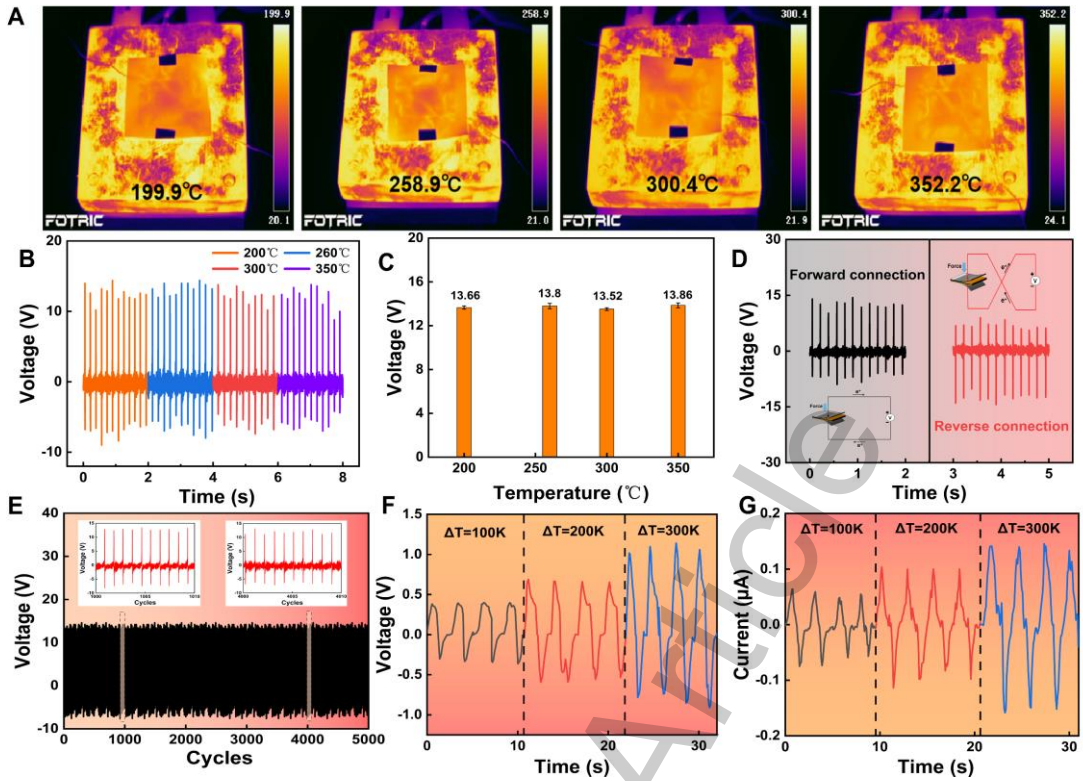

Figure 4. Electrical properties of PAN/$Zr(OAc)_4$ composite membranes for high-temperature resistant sensors at a heat treatment temperature of 450 °C. (A) High-temperature thermogram; (B) Piezoelectric output of the composite membrane at 200 °C, 260 °C, 300 °C, and 350 °C; (C) Piezoelectric output error bars; (D) Polarity reversal test at 400 °C; (E) Stability test of 5000 knock cycles at 400 °C. Pyroelectric properties of PAN/$Zr(OAc)_4$ composite membrane high-temperature resistant sensors: (F) Dependence of open-circuit voltage and (G) short-circuit current.

Table 2. Summary of electrical properties of PAN/$Zr(OAc)_4$ membranes at different heat-treatment temperatures

Heat-treated Temperature (℃)	Voltage(V)	Current(μA)	ε_r	P_r(μC/cm²)	d_{33}(P_c/N)
Untreated	4.04	0.097	4.282	0.421	3.190
50	4.28	0.122	-	-	-
100	4.68	0.151	-	-	-
150	5.16	0.176	4.609	0.515	4.19
200	5.48	0.203	-	-	-
250	6.12	0.217	-	-	-

Accepted Article

260	8.5	0.265	4.876	0.731	6.313
300	8.84	0.277	-	-	-
350	8.94	0.286	5.270	0.781	7.292
400	12.7	0.343	-	-	-
450	12.9	0.351	6.413	0.875	9.942
500	10.5	0.260	-	-	-
550	6.4	0.212	7.302	0.523	6.767

In addition, for the purpose of validating the mechanical stability of the fabricated PAN/$Zr(OAc)_4$ composite nanofiber membranes in high-temperature environments, a large number of cyclic knock and release tests were performed. From Figure 4E, the thin-membrane sensors were tested with 5,000 cycles under a force of 8 N at a frequency of 10 Hz in a 400 °C environment, and it was found that there was no obvious fluctuation or attenuation of the output performance, which indicates that the PAN/$Zr(OAc)_4$ membrane sensors have excellent mechanical stability even in high-temperature environments. The results show that the prepared PAN/$Zr(OAc)_4$ membranes, after being encapsulated with high-temperature-resistant materials, have excellent electrical output, mechanical stability, and high-temperature-resistant properties that can enable them to be widely used for energy harvesting or real-time monitoring of data in high-temperature fields, such as aerospace, industrial production, energy, and automobile engines.

Since heat-treated PAN has pyroelectric properties, the pyroelectric properties of PAN/$Zr(OAc)_4$ composite nanofiber membrane sensors heat-treated at 450 °C were investigated, the mechanism of the fabricated sensor to sense temperature as shown in Supplementary Figure 7. During the testing, the distance between the sensor and the heat source was strictly controlled (gradually shortened from 30 cm to 5 cm), and the time was controlled at about 2s. It was used to test the pyroelectric output performance of the PAN/$Zr(OAc)_4$ membrane sensors at different temperature gradients (ΔT = 100 K, 200 K, and 300 K, representing the temperature change from room temperature to the displayed temperature). The results are shown in Figure 4F and G, where the pyroelectric output voltage and current of the PAN/$Zr(OAc)_4$ membrane sensors are gradually enhanced with the increase of the test temperature. In addition, to rule out the effects of thermomechanical or frictional electrification in pyroelectric measurements, a series of

Accepted Article

control experiments were conducted, and the results are shown in the Supplementary Figure 8. This confirms that the PAN/$Zr(OAc)_4$ membrane sensor has good temperature sensitivity and fast response characteristics. The pyroelectric current (I_{pyro}) can be calculated by equation (4):

$$I_{pyro} = pA\frac{dT}{dt} \quad (4)$$

where p is the pyroelectric coefficient, A is the effective area of the fiber membrane, and dT/dt is the temperature change rate. Supplementary Figure 8C and 8D show the Changes in temperature and Corresponding differential curve of the PAN/$Zr(OAc)_4$ composite menbrane sensor. The pyroelectric output current was then fitted to the temperature gradient [Supplementary Figure 8E], revealing a linear correlation between the output current and the temperature gradient. Based on the fitted curve of output current versus temperature gradient, the temperature resolution was determined to be 1.51 nA/°C. As the temperature change gradient (ΔT) rose from 100 K to 300 K, both of their pyroelectric responses were significantly enhanced. This enables PAN/$Zr(OAc)_4$ membrane sensors to achieve sensing monitoring of changes in heat sources through temperature gradient changes, which are used to monitor and protect devices operating in high-temperature environments from localized over-temperature and reduced device lifetime. To achieve the selection of pyroelectric and piezoelectric outputs in practical applications, the two signals can be used independently according to the measured target. The pyroelectric signal is used for temperature monitoring, while the piezoelectric signal is used for mechanical detection. The pyroelectric and piezoelectric responses can be effectively decoupled and superimposed under different signals as shown in Supplementary Figure 9, demonstrating reliable dual-mode sensing performance.

Critical components in automobile engine [Figure 5A], such as cylinder walls, exhaust pipe interfaces and turbochargers are prone to material fatigue, seal aging and even structural deformation due to localized overheating (> 400 ℃) during prolonged high-load operation, which significantly shortens the service life. The high temperature monitoring and warning is crucial for extending the service life of automobile engines and ensuring the safety of passengers. Traditional temperature monitoring methods, such as thermocouples are difficult to fit curved or irregular components due to their rigid

Accepted Article

construction and are susceptible to contact failure under vibration. Owing to excellent flexibility (intimate conformity to complex curved surface), outstanding high-temperature resistance (stable operation above 500 °C) and good sensitivity to temperature (linear pyroelectric response characteristics) of PAN/$Zr(OAc)_4$ membrane sensor prepared in this study. we offer an effective solution for real-time temperature monitoring of engines operating in high temperature environment. The PAN/$Zr(OAc)_4$ membrane sensors were attached to the engine cylinder wall surface as shown in Figure 5B and C, and the corresponding pyroelectric output voltages were measured under different temperature gradients. The pyroelectric output voltage results of PAN/$Zr(OAc)_4$ membrane sensor are presented in Figure 5D. From Figure 5D, and it was found that the pyroelectric outputs increased with the temperature gradient increasing, the pyroelectric output voltages were 0.39, 0.52, 0.7, 0.8, 0.98, 1.09,1.22 and 1.37 V at the temperature gradients of 100,150, 200,250, 300, 350, 400, and 450 ºC, respectively. A fitted curve of the output voltage versus temperature gradient was plotted 355.98 °C/V sensitivity, as shown in Figure 5E. The sensor was subjected to 30 thermal cycles at the threshold temperature of 400 °C, the pyroelectric output remained stable. Furthermore, the hysteresis characteristic was studied by recording the voltage during heating and cooling processes. The heating and cooling curves almost overlap, indicating a small hysteresis and good repeatability of the sensor. These results confirm that the prepared pyroelectric sensor possesses satisfactory sensitivity, stability, and hysteresis performance for real-time engine temperature monitoring. A graphical user interface (GUI) was developed in Python simulation software based on PyQt module suite to visualize local temperature variations in real time. A threshold temperature of 400 °C was set for safety monitoring, The GUI is then used to monitor and display the variation of the local temperature of the engine. When the temperature at any of the monitoring points below 400°C, the indicator light is green indicating normal engine temperature [Figure 5F]. When the temperature reaches the 400 °C threshold [Figure 5G], the interface alarm indicator turns red to alert the driver to perform maintenance. Additionally, considering quantitative analysis of localized temperature monitoring on engine surfaces, the response time of PAN/$Zr(OAc)_4$ composite nanofiber sensors was tested at different engine temperatures with a spatial resolution of 1.5 × 1.5 cm^2. As shown in Supplementary Figure 10, the trigger response time of the pyroelectric sensor gradually accelerated as localized engine temperatures increased, reaching 0.6 s when the local temperature reached 400°C.

Accepted Article

Furthermore, when the local temperature reached 450°C, eight cyclic tests were conducted. The trigger events remained stable at approximately 0.21 s without significant fluctuation, indicating that the prepared pyroelectric sensor exhibits both sensitive responsiveness and stability during temperature monitoring. This intelligent monitoring system not only prolongs the service life of critical engine components but also optimizes fuel efficiency through precise temperature control, providing a reliable and stable technical solution for monitoring thermal safety in extreme environments in the automotive industry. Furthermore, by adjusting the threshold temperature, the system can be readily adapted for thermal monitoring in other high-temperature scenarios, demonstrating its broad potential for applications in extreme thermal environments.

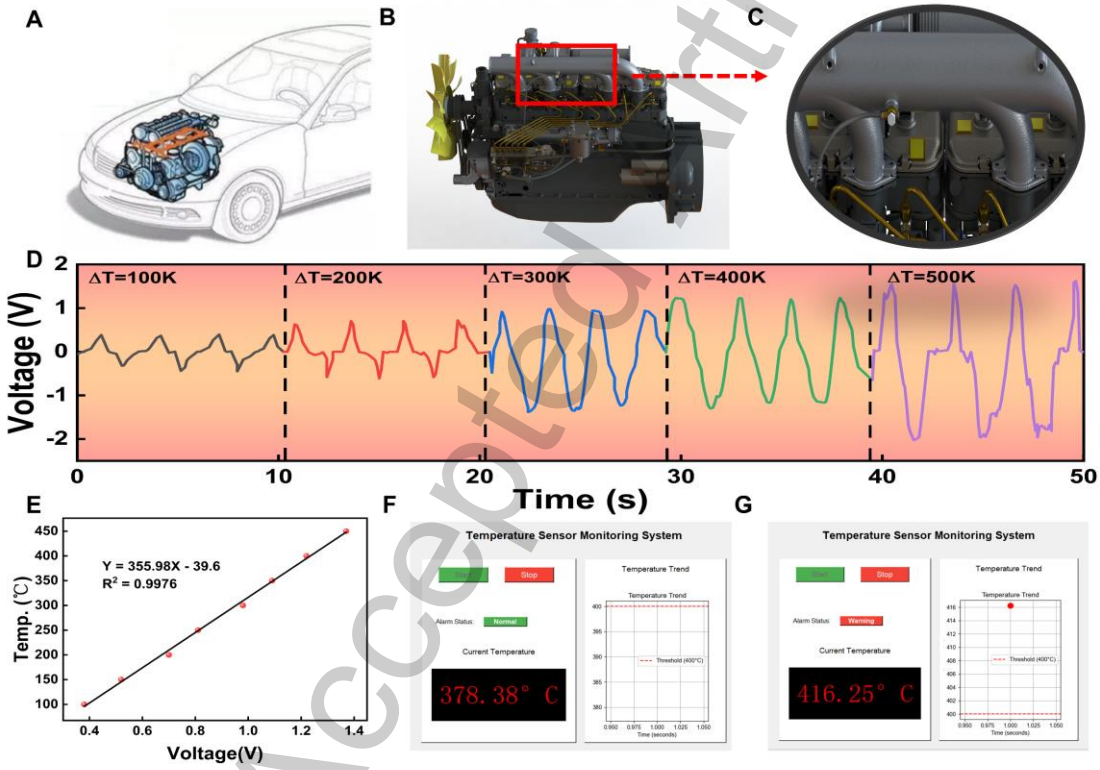

Figure 5. (A) Diagram of an automobile engine model. (B) Model engine diagram of pasted PAN/$Zr(OAc)_4$ composite nanofiber membrane sensor and (C) local magnification sensor output interface temperature display. (D) Pyroelectric output of 450 °C heat-treated PAN/$Zr(OAc)_4$ membrane sensor for different heat source temperature gradients (ΔT = 100, 200, 300, 400, 500 K). (E) Fitted curve of pyroelectric output voltage as a function of temperature gradient. (F) Local temperature normal and (G) local temperature too high.

Accepted Article

CONCLUSIONS

In this study, we developed a flexible, high-temperature-resistant nanofiber sensor with dual piezo/pyroelectric functionalities based on a PAN/$Zr(OAc)_4$ composite, aiming to address the need for stable, high-performance sensing in extreme thermal environments. The fabricated PAN/$Zr(OAc)_4$ composite nanofiber sensor exhibited excellent flexibility, enhanced mechanical strength, and stable dual piezo/pyroelectric functionality, with $Zr(OAc)_4$ incorporation and optimized heat treatment significantly boosting its electrical output and thermal endurance. This sensor (heat-treated at 450 °C) has a maximum open-circuit voltage of 12.9 V and a short-circuit current of 0.351 μA at room temperature, and the output voltage of the heat treatment PAN/$Zr(OAc)_4$ nanofiber film (450 ℃) in a high-temperature environment (below its heat treatment temperature) was 14.1V. Furthermore, the PAN/$Zr(OAc)_4$ composite nanofiber sensor maintained stable performance even after more than 10,000 room-temperature cycles and 5,000 high-temperature cycles. The pyroelectric effect of the heat-treated composite enabled linear, real-time temperature monitoring, demonstrating its potential for practical thermal sensing applications. With its superior high-temperature resistance, dual functionality, and long-term stability, the PAN/$Zr(OAc)_4$ composite nanofiber sensor holds great promise for thermal monitoring and energy harvesting in extreme environments such as aerospace, oil drilling, and new energy systems.

DECLARATIONS

Authors' contributions

Writing - original draft, Visualization, Validation, Methodology, Investigation, Formal analysis, Data curation, Conceptualization: Fan, K.; Li, Y.

Validation, Investigation: Li, Q.; Sun, J.; Jin, Y.; Li, G.; Liang, J.; Zhou, Y.

Supervision, Funding acquisition: Li, Y.; Bian, G.

Review & editing, Supervision: Huang, Y.; Li, Y.

Availability of data and materials

The authors declare that the primary data supporting the findings of this study are available within the paper and its Supplementary Materials. Additional data are available from the corresponding authors upon reasonable request.

Accepted Article

AI and AI-assisted tools statement

AI-assisted tools were used for language polishing and translation assistance during manuscript preparation. The research content, experimental data, conclusions, and academic viewpoints are independently completed by the authors, who take full responsibility for intellectual property and academic integrity.

Financial support and sponsorship

This work was supported by National Natural Science Foundation of China (Grant No.52427809, No. 52205593, No.62525311), Major Science and Technology Project of Shanxi Province (20201102003), Shanxi Province Science Foundation for Youths (Grant No. 20210302124046), Key Research and Development Special Projects of Lvliang city and University cooperation (Grant No. 2022XDHZ08), Open Project of State Key Laboratory of Intelligent Manufacturing Equipment and Technology (IMETKF2025016).

Conflicts of interest

Huang, Y. serves as the Editor-in-Chief of the journal *Soft Science*; however, he was not involved in any stage of the editorial process for this manuscript, including reviewer selection, manuscript handling, or decision-making. The other authors declare that they have no conflicts of interest.

Ethical approval and consent to participate

Not applicable.

Consent for publication

Not applicable.

Copyright

© The Author(s) 2026.

Accepted Article

REFERENCES

1. Liu, Z. J.; Tian, B.; Jiang, Z. D.; et al. Flexible temperature sensor with high sensitivity ranging from liquid nitrogen temperature to 1200° C. *International Journal of Extreme Manufacturing*. **2022**, *5*, 015601. DOI: 10.1088/2631-7990/aca44d

2. Liu, Y. H.; Wang, J. L.; Liu, T.; et al. Triboelectric tactile sensor for pressure and temperature sensing in high-temperature applications. *Nat. Commun.* **2025**, *16*, 383. DOI: 10.1038/s41467-024-55771-0
3. Li, Y.; Zhu, Z.; Wen, C.; et al. Rub-impact dynamic analysis of a dual-rotor system with bolted joint structure: theoretical and experimental investigations. *Mech. Syst. Signal Pr.* **2024**, *209*, 111144. DOI: 10.1016/j.ymssp.2024.111144
4. Liu, H.; Sun, J. Z.; Lei, S. Y.; et al. In-service aircraft engines turbine blades life prediction based on multi-modal operation and maintenance data. *Propuls. Power Res.* **2021**, *10*, 360-373. DOI: 10.1016/j.jppr.2021.09.001
5. Zhang, X. Y.; Wang, Y.; Gao, X. Y.; et al. High-temperature and flexible piezoelectric sensors for lamb-wave-based structural health monitoring. *ACS Appl. Mater. Interfaces*. **2021**, *13*, 47764-47772. DOI: 10.1021/acsami.1c13704
6. Chen, S. Y.; Bai, C.; Zhang, C. Y.; et al. Flexible piezoresistive three-dimensional force sensor based on interlocked structures. *Sensor. Actuat. A-Phys*. **2021**, *330*, 112857. DOI: 10.1016/j.sna.2021.112857
7. Chen, X.; Wang, Y. R.; Zhang, J. Y.; et al. Three-dimensional micro strain gauges as flexible, modular tactile sensors for versatile integration with micro- and macroelectronics. *Sci. Adv.* **2024**, *10*, eadp6094. DOI: 10.1126/sciadv.adp6094
8. Bangul, K.; Umay, A.; Bilawal, K.; et al. Next-generation piezoelectric materials in wearable and implantable devices for continuous physiological monitoring. *Adv. Sci.* **2025**, *12*, e07853. DOI: 10.1002/advs.202507853
9. Li, M. L.; Li, Z.; Yaseen, S.; et al. High performance piezoelectric nanogenerator based on aligned single crystal $BaTiO_3$ nanowires for self-powered applications. *Chem. Eng. J.* **2025**, *516*, 163834. DOI: 10.1016/j.cej.2025.163834
10. Kumar, M.; Kulkarni, N. D.; Kumari, P. Piezoelectric performance enhancement of electrospun functionally graded PVDF/$BaTiO_3$ based flexible nanogenerators. *Mater. Res. Bull.* **2024**, *174*, 112739. DOI: 10.1016/j.materresbull.2024.112739
11. Yuan, L. J.; Fan, W.; Yang, X.; et al. Piezoelectric PAN/$BaTiO_3$ nanofiber membranes sensor for structural health monitoring of real-time damage detection in composite. *Compos. Commun.* **2021**, *25*, 100680. DOI: 10.1016/j.coco.2021.100680
12. David, K.; Abhinav, G.; Sahana, V.; et al. A gas ionization sensor with a novel pyroelectric lithium niobate crystal as a voltage source. *Sensor. Actuat. A-Phys.* **2025**, *389*, 116544. DOI: 10.1016/j.sna.2025.116544

Accepted Article

13. Wang, G. L.; Wang, F. L.; Gao, X.; et al. Near stoichiometric lithium niobate crystal with dramatically enhanced piezoelectric performance for high-temperature acceleration sensing. *J. Mater. Chem. C*. **2024**, *12*, 16357-16366. DOI: 10.1039/d4tc02466d
14. Dagdeviren, C.; Su, Y.; Joe, P.; et al. Conformable amplified lead zirconate titanate sensors with enhanced piezoelectric response for cutaneous pressure monitoring. *Nat. Commun.* **2014**, *5*, 4496. DOI: 10.1038/ncomms5496
15. Yuan, Y. L.; Gao, L.; Li, N. X.; et al. Bottom electrode effects on piezoelectricity of $Pb(Zr_{0.52},Ti_{0.48})O_3$ thin film in flexible sensor applications. *Materials*. **2023**, *16*, 10. DOI: 10.3390/ma16237470
16. Sun, Y.; Liu, D. L.; Li, Q.; et al. Piezoelectric property of a tetragonal (Ba, Ca)(Zr, Ti) O_3 single crystal and its fine-domain structure. *ACS Appl. Mater. Interfaces*. **2018**, *10*, 12847-12853. DOI: 10.1021/acsami.8b01360
17. Costa, C. M.; Cardoso, V. F.; Martins, P.; et al. Smart and multifunctional materials based on electroactive poly (vinylidene fluoride): recent advances and opportunities in sensors, actuators, energy, environmental, and biomedical applications. *Chem. Rev*. **2023,** *123***,** 11392-11487. DOI: 10.1021/acs.chemrev.3c00196
18. Peng, R. B.; Zhang, B. T.; Dong, G. H.; et al. Enhanced piezoelectric energy harvester by employing freestanding single-crystal $BaTiO_3$ films in PVDF-TrFE based composites. *Adv. Funct. Mater.* **2024**, *34*, 2316519. DOI: 10.1002/adfm.202316519
19. Zhang, H.; Zhang, X. X.; Qiu, C. K.; et al. Polyaniline/ZnO heterostructure-based ammonia sensor self-powered by electrospinning of PTFE-PVDF/MXene piezo-tribo hybrid nanogenerator. *Chem. Eng. J.* **2024**, *496*, 154226. DOI: 10.1016/j.cej.2024.154226
20. Qian, F.; Jia, R. Y.; Cheng M. D.; Chaudhary, A.; et al. An overview of polylactic acid (PLA) nanocomposites for sensors. *Adv. Compos. Hybrid Ma.* **2024**, *7*, 75. DOI: 10.1007/s42114-024-00887-6
21. Li, Z. Y.; Li, J. R.; Wu, B.; et al. Interfacial-engineered robust and high performance flexible polylactic acid/polyaniline/MXene electrodes for high-perfarmance supercapacitors. *J. Mater. Sci. Technol.* **2024**, *203*, 201-210. DOI: 10.1016/j.jmst.2024.02.084
22. Peng, W.; Wang L. T.; Zhang, M. Y.; et al. Biodegradable flexible conductive film based on sliver nanowires and PLA electrospun fibers. *J. App.l Polym. Sci.* **2024**,

Accepted Article

141, e55433. DOI: 10.1002/app.55433

23. Zhao, X. P.; Yu, J. J.; Wang, X.; et al. Strong synergistic toughening and compatibili--zation enhancement of carbon nanotubes and multi-functional epoxy compatibilizer in high toughened polylactic acid (PLA)/poly (butylene adipate-co-terephthalate)(PBAT) blends. *Int. J. Biol. Macromol.* **2023**, *250*, 126204. DOI: 10.1016/j.ijbiomac.2023.126204
24. Azimi, B.; Milazzo, M.; Lazzeri, A.; et al. Electrospinning piezoelectric fibers for biocompatible devices. *Adv. Healthc. Mater.* **2020**, *9*, 1901287. DOI: 10.1002/adhm.201901287
25. Lee, H. J.; Zhang, S. Design of low-loss 1-3 piezoelectric composites for high-power transducer applications. *IEEE T. Ultrason. Ferr.* **2012**, *59*, 1969-1975. DOI: 10.1109/TUFFC.2012.2415
26. Jian, G.; Jiao, Y.; Meng, Q. Z.; et al. Excellent high-temperature piezoelectric energy harvesting properties in flexible polyimide/3D $PbTiO_3$ flower composites. *Nano Energy*. **2021**, *82*, 105778. DOI: 10.1016/j.nanoen.2021.105778
27. Hyeon, D. Y.; Lee, G. J.; Lee, S. H.; et al. High-temperature workable flexible piezoelectric energy harvester comprising thermally stable (K, Na) NbO_3-based ceramic and polyimide composites. *Compos. Part B-Eng.* **2022**, *234*, 109671. DOI: 10.1016/j.compositesb.2022.109671
28. Zhang, X. Y.; Wang, Y.; Shi, X. N.; et al. Heteroepitaxy of flexible piezoelectric Pb ($Zr_{0.53}Ti_{0.47}$) O_3 sensor on inorganic mica substrate for lamb wave-based structural health monitoring. *Ceram. Int.* **2021,** *47*, 13156-13163. DOI: 10.1016/j.ceramint.2021.01.180
29. Kaur, G.; Sharma, A. K.; Jassal, M.; Agrawal, A. K. ZnO-poly (acrylonitrile) composite films with improved piezoelectric properties for energy harvesting and sensing applications. *Compos. Sci. Technol.* **2023**, *243*, 110260. DOI: 10.1016/j.compscitech.2023.110260
30. Wang, W. Y.; Zheng, Y. D.; Sun, Y.; et al. High-temperature piezoelectric conversion using thermally stabilized electrospun polyacrylonitrile membranes. *J. Mater. Chem. A*. **2021**, *9*, 20395-20404. DOI: 10.1039/d1ta04400a
31. Klinar, K.; Law, J. Y.; Franco, V.; Moya, X.; et al. Perspectives and energy applications of magnetocaloric, pyromagnetic, electrocaloric, and pyroelectric materials. *Adv. Energy. Mater.* **2024**, *14*, 36. DOI: 10.1002/aenm.202401739

Accepted Article

32. Yin, R. Y.; Li, Y. H.; Li W. D.; et al. High-temperature flexible electric Piezo/pyroelectric bifunctional sensor with excellent output performance based on thermal-cyclized electrospun PAN/Zn $(Ac)_2$ nanofiber mat. *Nano Energy*. **2024**, *124,* 109488. DOI: 10.1016/j.nanoen.2024.109488
33. Li, Y. H.; Tan, J. Q.; Liang, K.; et al. Enhanced piezoelectric performance of multi-layered flexible polyvinylidene fluoride–$BaTiO_3$–rGO films for monitoring human body motions. *J. Mater. Sci.: Mater. Electron.* **2022**, *33*, 4291-4304. DOI: 10.1007/s10854-021-07622-7
34. Dang, W.; Liu, J.; Wang X. X.; et al. Structural transformation of polyacrylonitrile (PAN) fibers during rapid thermal pretreatment in nitrogen atmosphere. *Polymers*. **2020**, *12*, 63. DOI: 10.3390/polym12010063
35. Chao, H. W.; Hsu, H. C.; Chen, Y. R.; Chang, T. H. Characterizing the dielectric properties of carbon fiber at different processing stages. *Sci. Rep.* **2021**, *11*, 17475. DOI: 10.1038/s41598-021-96949-6
36. Zhang, W.; Sun, Q.; Shen, Z. G.; Liu, J.; et al. Effect of diameter on the structural evolution and tensile properties of electrospun PAN-based carbon nanofiber mats. *ACS omega*. **2023**, *8*, 19002-19005. DOI: 10.1021/acsomega.3c01708
37. Love-Baker, C. A.; Harrell, T. M.; Vautard, F.; et al. Analysis of the turbostratic structures in PAN-based carbon fibers with wide-angle x-ray diffraction. *Carbon*. **2024**, *224*, 119037. DOI: 10.1016/j.carbon.2024.119037
38. Podder, S.; Nath, A. M.; Mukherjee, C.; et al. Fabrication and characterization of sol–gel-based coatings on quartz glass to obtain antireflective effect at 1054 nm for optics of high power Nd: phosphate glass laser. *B. Mater. Sc.* **2022**, *45*, 154. DOI: 10.1007/s12034-022-02732-2
39. Zeng, J. B.; Zhao, G. Z.; Liu, J. H.; et al. Interaction between thermal stabilization temperature program, oxidation reaction, and mechanical properties of polyacrylonitrile (PAN) based carbon fibers. *Diam. Relat. Mater.* **2024**, *141*, 110588. DOI: 10.1016/j.diamond.2023.110588
40. Liu, Y.; Liu, Y.; Shang, L.; Ao, Y. H. Study on the structural evolution of polyacrylonitrile fibers in stepwise heat treatment process and its relationship with properties. *J. Appl. Polym. Sci.* **2022**, *139*, 52077. DOI: 10.1002/app.52077
41. Zhou, H.; Zhu, J.; Wang, H. L. Tuning of structural/functional feature of carbon fibers: new insights into the stabilization of polyacrylonitrile. *Polymer*. **2023**, *282*, 126157. DOI: 10.1016/j.polymer.2023.126157

Accepted Article

42. He, Z. P.; Liu, H. C.; Zhang, S.; et al. Investigation of the cyclization mechanism of poly (acrylonitrile-co-ethylenesulfonic acid) copolymer during thermal oxidative stabilization by in situ infrared spectroscopy. *Ind. Eng. Chem. Res.* **2020**, *59*, 9519-9531. DOI: 10.1021/acs.iecr.0c00977
43. Sun, Y.; Liu, Y.; Zheng, Y.; et al. Enhanced energy harvesting ability of ZnO/PAN hybrid piezoelectric nanogenerators. *ACS Appl. Mater. Interfaces*. **2020**, *12*, 54936-54945. DOI: 10.1021/acsami.0c14490
44. Liu, J.; Zhang, W. X. Structural changes during the thermal stabilization of modified and original polyacrylonitrile precursors. *J. Appl. Polym. Sci.* **2005**, *97*, 2047-2053. DOI: 10.1002/app.21916
45. Ahn, H.; Yeo, S. Y.; Lee, B. S. Designing materials and processes for strong polyacrylonitrile precursor fibers. *Polymers*. **2021**, 13, 2863. DOI: 10.3390/polym13172863
46. Zhang, X. Y.; Kitao, T.; Nishijima, A.; Uemura, T. Thermal transformation of polyacrylonitrile accelerated by the formation of ultrathin nanosheets in a metal–organic framework. *ACS Macro. Lett.* **2023**, *12*, 415-420. DOI: 10.1021/acsmacrolett.3c00072
47. Zeng, W. R.; Liu, L.; Shen, Y. Z.; et al. Conformational selection of polymer chains upon π- π interactions with small molecules. *Phys. Rev. Lett.* **2024**, *133*, 178101. DOI: 10.1103/PhysRevLett.133.178101
48. Konstantopoulos, G.; Soulis, S.; Dragatogiannis, D.; Charitidis, C. Introduction of a methodology to enhance the stabilization process of PAN fibers by modeling and advanced characterization. *Materials*. **2020**, *13*, 2749. DOI: 10.3390/ma13122749
49. Ju, A.; Guang, S.; Xu, H. Effect of comonomer structure on the stabilization and spinnability of polyacrylonitrile copolymers. *Carbon*. **2013**, *54*, 323-335. DOI: 10.1016/j.eurpolymj.2024.112931
50. Kissinger, H. E. Reaction kinetics in differential thermal analysis. *Anal. Chem.* **1957**, *29*, 1702-1706.
51. Valdez, S.; Qiang, Z. Understanding Non-isothermal Crystallization Behaviors of Polyethylene-Derived Vitrimers. *Macromolecules*. **2025**, *58*, 9348−9357. DOI: 10.1021/acs.macromol.5c01725.
52. Tabbagh, A.; Souffaché, B.; Jougnot, D.; et al. Experimental and numerical analysis of dielectric polarization effects in near-surface earth materials in the 100 Hz–10

Accepted Article

MHz frequency range: First interpretation paths. *Near. Surf. Geophys.* **2024**, *22*, 468-481. DOI: 10.1002/nsg.12302

53. Li, J. X.; Zhao, J.; Xu, Z.; Zhai, Y. L.; et al. High-temperature-resistant dual-scale ceramic nanofiber films toward improved air filtration. *ACS Appl. Mater. Interfaces*. **2024**, *16*, 60608-60615. DOI: 10.1021/acsami.4c15332
54. Pan, F.; Cai, L.; Shi, Y. Y.; et al. Heterointerface Engineering of β-Chitin/Carbon Nano-Onions/Ni–P Composites with Boosted Maxwell-Wagner-Sillars Effect for Highly Efficient Electromagnetic Wave Response and Thermal Management. *Nano-Micro Lett.* **2022**, *14*, 85. DOI: 10.1007/s40820-022-00804-w
55. Liu, L. S.; Yi, J. J.; Xu, K.; et al. High piezoelectric property with exceptional stability in self-poled ferroelectric films. *Nat. Commun.* **2024**, *15*, 10798. DOI: 10.1038/s41467-024-54707-y
56. Ye, J. K.; Ding, G. Y.; Wu, X. Y.; et al. Development and performance research of PSN-PZT piezoelectric ceramics based on road vibration energy harvesting technology. *Mater. Today Commun.* **2023**, *34*, 105135. DOI: 10.1016/j.mtcomm.2022.105135
57. Pan, D. M. Lead zirconate titanate (PZT) piezoelectric ceramics: Applications and prospects in human motion monitoring. *Ceram.-Silikaty*. **2024**, *68*, 444-458. DOI: 10.13168/cs.2024.0044
58. Kim, N. I.; Chang, Y. L.; Chen, J.; et al. Piezoelectric pressure sensor based on flexible gallium nitride thin film for harsh-environment and high-temperature applications. *Sensor. Actuat. A-Phys.* **2020**, *305*, 111940. DOI: 10.1016/j.sna.2020.111940
59. Liu, S. L.; Hu, S. T.; Wu, Q. F.; et al. Highly sensitive flexible high-temperature sensor based on ITO/In_2O_3 for underwater hot spring monitoring. *Sci. China Mater.* **2025**, *51*, 26892-26901. DOI: org/10.1007/s40843-025-3481-5
60. He, P. F.; Li, J. W.; Zhang, B. L.; et al. Mechanically robust porous polyimide films for piezoelectric sensing at extreme condition. *Compos. Sci. Technol.* **2025**, *261*, 111006. DOI: 10.1016/j.compscitech.2024.111006

Accepted Article